



**Numerical model of
mid-ocean ridges**

P. Machetel and
C. J. Garrido

Numerical model of crustal accretion and cooling rates of fast-spreading mid-ocean ridges

P. Machetel¹ and C. J. Garrido²

¹Géosciences Montpellier, UMR5243, CNRS-UM2, cc49, 34095 Montpellier cedex 05, France

²Instituto Andaluz de Ciencias de la Tierra (CSIC), Avenida de la Palmeras 4 Armilla, 18100, Granada, Spain

Received: 15 March 2013 – Accepted: 26 March 2013 – Published: 10 April 2013

Correspondence to: P. Machetel (philippe.machetel@laposte.net)

Published by Copernicus Publications on behalf of the European Geosciences Union.

Title Page

Abstract

Introduction

Conclusions

References

Tables

Figures



Back

Close

Full Screen / Esc

Printer-friendly Version

Interactive Discussion



Abstract

We designed a thermo-mechanical model for fast spreading mid-ocean ridge with variable viscosity, hydrothermal cooling, latent heat release, sheeted dyke layer, and variable melt intrusion possibilities. The model allows to take into account several accretion possibilities as: the “gabbro glacier” (G), the “sheeted sills” (S) or the “mixed shallow and MTZ lenses” (M). Viscosity contrasts of 2 to 3 orders of magnitude between the hot and cold phases have been tested. We also explored hydrothermal cooling according to various cracking temperatures for crustal rocks. Hence, the model allows exploring various near ridge motions and thermal patterns that induce various cooling histories for gabbros. According to the assumed opening-closure temperature range, the cooling rates sample the near-ridge structure or record areas farther from the ridge. As an analogy to experimental petrology we called ICR the cooling rates sampled near the ridge and SRC the cooling rates sampled far from the ridge where the flow tends to laminar and conductive patterns. The results emphasize that the cooling rates may significantly depend on the choice of this opening-closure temperature range. The results show that numerical modeling of thermo-mechanical properties of the lower crust’s may bring information to study the hypotheses related to the ridge accretion structure, hydrothermal cooling and thermal state at the fast-spreading ridges.

1 Introduction

There remain uncertainties in how the oceanic crust is accreted at fast mid-ocean ridges, both in terms of accretion geometry but also in terms of roles and efficiencies of the cooling processes like hydrothermal convective circulation. During the last decades, three main families of structures have been proposed to take into account the local thermal, seismic or geophysics properties of the mid-ocean ridges. Thus, Norman Sleep (1975) proposed a “gabbro glacier” (henceforth “G structure”) mechanism where crystallization, occurs below the sheeted dykes at the floor level of a shallow

GMDD

6, 2429–2456, 2013

Numerical model of mid-ocean ridges

P. Machetel and
C. J. Garrido

Title Page

Abstract

Introduction

Conclusions

References

Tables

Figures



Back

Close

Full Screen / Esc

Printer-friendly Version

Interactive Discussion



Numerical model of mid-ocean ridges

P. Machel et al.
C. J. Garrido

Title Page

Abstract

Introduction

Conclusions

References

Tables

Figures

⏪

⏩

◀

▶

Back

Close

Full Screen / Esc

Printer-friendly Version

Interactive Discussion



melt lens. Gabbros flow downward and outward to build the entire lower oceanic crust below the sheeted dykes. This ridge structure is compatible with the geophysical observations collected at the East Pacific Rise (EPR) and also with the structural studies of the Oman ophiolite (Nicolas et al., 1988; Kent et al., 1990; Sinton and Detrick, 1992; Henstock et al., 1993; Nicolas et al., 1993; Quick and Denlinger, 1993; Phipps Morgan and Chen, 1993). However, it seems that other geophysical measurements at the EPR (Crawford and Webb, 2002; Dunn et al., 2000; Nedimovic et al., 2005) and field observations from the Oman ophiolite (Kelemen et al., 1997; Korenaga and Kelemen, 1997) also suggest mixed accretion mechanisms (“M structures”) that involve melt lenses at both shallow depth and Moho Transition Zone (MTZ) (Boudier and Nicolas, 1995; Schouten and Denham, 1995; Boudier et al., 1996; Chenevez et al., 1998; Chen, 2001). Furthermore, several authors (Bédard and Hebert, 1996; Kelemen et al., 1997; Korenaga and Kelemen, 1997; Kelemen and Aharonov, 1998; MacLeod and Yaouancq, 2000; Garrido et al., 2001) argue in favor of melt intrusions at various depths through superimposed sills at the ridge axis between the Moho and the upper lens (S structure).

A lively scientific debate opposes these three possibilities according to their effects on the thermal structure near the ridge. Indeed Chen (2001) argued against the M and S propositions observing that the latent heat release during crystallization would melt the lower crust if a significant quantity of gabbro were generated deep in the crust without efficient extraction of heat from the hot/ductile crust by efficient hydrothermal cooling. However, the scientific debate about the depth and the temperature for which hydrothermal cooling remains also still open with opinions that it may even be efficient until Moho, consistently with the seismic observations at EPR (Dunn et al., 2000). The depth where hydrothermal convective processes cool the lower crust is related to the thermal cracking temperature of peridotite that depends on cooling rates, grain sizes, confining pressures and viscoelastic transition temperatures (DeMartin et al., 2004). A review of this question has been proposed by Theissen-Krah et al. (2011), with a cracking temperature ranging from 400 °C to 1000 °C. Hence, analyzing high

**Numerical model of
mid-ocean ridges**P. Machetel and
C. J. Garrido

Title Page

Abstract

Introduction

Conclusions

References

Tables

Figures

◀

▶

◀

▶

Back

Close

Full Screen / Esc

Printer-friendly Version

Interactive Discussion



temperature hydrothermal veins (900–1000 °C), Bosch et al. (2004) found hydrous alterations of gabbro active above 975 °C requiring hydrothermal circulations until the Moho. Theirs results are in agreement with those of Koepke et al. (2005), which have proposed hydrothermal activity of the deep oceanic crust at very high temperature (900–1000 °C) and with those of Boudier et al. (2000), which proposed a temperature cracking higher than the gabbro solidus. Conversely, Coogan et al. (2006), bounds the hydrothermal flows in the near-axis plutonic complex of Oman ophiolite at a temperature of 800 °C, in agreement with the model of Cherkaoui et al. (2003). This very exciting scientific debate let us motivate to improve a tool that may be useful exploring the effects of the melt accretion structures and hydrothermal cooling hypotheses on the near ridge thermal and dynamic patterns.

In this work we present a series of cases calculated from a numerical code written to explore the sensitivity of the ridge thermal and dynamic patterns versus the melt intrusion geometry and efficiency of hydrothermal cooling. Assessments of the feedback interactions between these two badly constrained processes are important to understand the long term properties of the ridge dynamics and to help to interpret the petrologic or geophysical observations. In the code, we have chosen to simulate hydrothermal cooling with an enhanced thermal conductivity triggered by threshold cracking temperatures. In the following of Chenevez et al. (1998), the numerical approach consistently solve the temperature and motion equations that are linked through thermal advection terms and temperature dependence of the viscosity. However Chenevez et al. (1998) did not open the possibility of other melt intrusion pattern than M structure. Later thermal models by Maclennan et al. (2004 and 2005) assumed melt intrusions at several positions rather than at the bottom ridge axis but without explicit coupling between motion and temperature equations. The present work is an improvement of Machetel and Garrido (2009) that opened the possibility of modulating the melt intrusion structure with a consistent solving of motion and temperature conservative equations. This new version of the code introduces the sheeted dyke layer that strongly modifies the thermal structure of the lower crust at shallow depth in a framework that also describes the

physical coupling of hydrothermal effects, temperature structure, crystallization, viscosity and ridge accretion structure.

2 Theoretical and numerical backgrounds

A global iterative process couples the solving of temperature and motion equations until reaching steady-state solutions, which can be used, in a second step, to compute the thermal histories of tracers along their cooling pathway in the lower crust. The basic equations, numerical methods and the internal and boundary conditions described by Machetel and Garrido (2009) have been changed to take into account the effects of a shallow sheeted dyke structure in the upper part of the oceanic crust. We think it justifies, improving the clarity of this paper, to present again a detailed description of these numerical and physical assumptions.

The program simulates the thermal and dynamical behaviors of two diverging lithospheric plates, and, although the code could incorporate asymmetric spreading and asymmetric modes of melt intrusion, the cases presented in this paper have been obtained with symmetric spreading plate velocities, $V_p = 50 \text{ mm yr}^{-1}$, and symmetric melt intrusions.

Three conservative principles have been applied to ensure the momentum, mass and energy conservations of the fluid. Within this framework, the classical equations of fluid mechanics include the effects and the interactions between the melt intrusions and the physical parameters describing latent heat releases, viscosity variations and hydrothermal cooling. The Boussinesq, mass conservation equation (Eq. 1) is written for an infinite Prandtl number, incompressible fluid (Machetel and Garrido, 2009).

$$\text{div} \mathbf{v} = 0 \tag{1}$$

The mathematical properties of this zero-divergence velocity field allow introducing a stream-function, ψ , from which it is possible to calculate the velocity components

Numerical model of mid-ocean ridges

P. Machetel and
C. J. Garrido

Title Page

Abstract

Introduction

Conclusions

References

Tables

Figures



Back

Close

Full Screen / Esc

Printer-friendly Version

Interactive Discussion



(Eq. 2).

$$v_x = \frac{\partial \psi}{\partial y}; \quad v_y = -\frac{\partial \psi}{\partial x} \quad (2)$$

However, the fluid motion has also to verify the conservation of momentum that links the body forces, the pressure and the stress tensor with the physical properties of the lower crust. From the physical values given in Table 1, the Prandtl number, $Pr = (c_p \eta) / k$ that characterizes the ratio of the fluid viscosity to the thermal conductivity, ranges between 2.5×10^{15} and 2×10^{18} . Such high values allow neglecting the inertial terms of the motion equation, which finally reduces to Eq. (3) following Chenevez et al. (1998).

$$\rho \mathbf{g} + \nabla \cdot \underline{\underline{\tau}} - \nabla p = 0 \quad (3)$$

In this equation, the stress tensor, τ , can be written as:

$$\underline{\underline{\tau}} = \eta(\nabla \mathbf{v} + \nabla \mathbf{v}^T). \quad (4)$$

Now, within this context, the crustal flow remains two-dimensional in a vertical plane parallel to the spreading direction. Then, the vorticity vector, $\boldsymbol{\omega} = \text{curl} \mathbf{v}$ has only one non-zero component and will be treated as a scalar value ω . After some mathematical transformations, it is possible to rewrite the continuity and momentum equations (Eqs. 1 and 3) in a system of two coupled stream-function and vorticity, Laplace equations (Eqs. 5 and 6) keeping all the terms that appear with the effects of a non-constant viscosity.

$$\nabla^2 \psi + \omega = 0 \quad (5)$$

$$\nabla^2(\eta \omega) = -4 \frac{\partial^2 \psi}{\partial x \partial y} \frac{\partial^2 \eta}{\partial x \partial y} - 2 \frac{\partial^2 \psi}{\partial x^2} \frac{\partial^2 \eta}{\partial y^2} - 2 \frac{\partial^2 \psi}{\partial y^2} \frac{\partial^2 \eta}{\partial x^2}. \quad (6)$$

Finally, the vorticity and stream-function equations need to be completed by one more equation checking the conservation of thermal energy. The terms of the temperature

GMDD

6, 2429–2456, 2013

Numerical model of mid-ocean ridges

P. Machellet and
C. J. Garrido

Title Page

Abstract

Introduction

Conclusions

References

Tables

Figures

⏪

⏩

◀

▶

Back

Close

Full Screen / Esc

Printer-friendly Version

Interactive Discussion



equation (Eq. 7) take into account the heat produced by viscous heating, the latent heat (according to the variations of the crystallization function Γ_c) and hydrothermal cooling (through an enhanced thermal conductivity).

$$\rho C_p \frac{d(T)}{dt} = \text{div} k \text{grad} T + \rho Q_L \frac{d\Gamma_c}{dt} + \tau_{ik} \frac{\partial v_i}{\partial x_k}. \quad (7)$$

5 The formalism described above offers two main advantages. The first is the numerical stability of the coupled elliptic, Laplace operators for ω and ψ . The second is the physical meaning of the stream function since local differences of its amplitude, between any two points of the calculation grid, measure the discharge ($\text{m}^3 \text{s}^{-1} \text{m}^{-1}$) of matter flowing between these points. As a direct mathematical consequence of Eq. (2), the isocon-

10 tours of ψ indicate directly the direction of the velocity vector. To set the geometry of the melt intrusion at the ridge axis we use the global properties of the mass conservation that requires the balance of the inflows (at the bottom ridge) and outflows (through the right and left lateral boundaries) (Fig. 1). Since the left and right spreading rates are equal, the amplitude of the stream-function jump at the bottom of the ridge axis is

15 $\psi_c = 2V_p H$. The stream-function being mathematically defined to an arbitrary constant, we have chosen to set the bottom left boundary value to $\psi_{lb} = 0.5\psi_c = V_p H$. Then, starting from this bottom left value for the stream-function boundary conditions and turning all around the box we can determine the other external boundary conditions according to the flows escaping or going in the box through these boundaries (Fig. 1). At the left

20 lateral boundary the stream-function decreases linearly: ($\psi_l = \psi_{lb} - y \cdot V_p$). It reaches $\psi_t = 0$ at the top, and, since no fluid can escape through the upper boundary, remains zero from the left to the right upper corners of the computation grid. Conversely, the stream function boundary conditions decreases linearly from zero at the upper surface, to $\psi_r = V_p(y - H)$ at depth y , and to $\psi_{rb} = -0.5\psi_c$ at the lower right corner along the right

25 lateral boundary. At the ridge, the pattern of the melt intrusion will be set thanks to internal conditions applied on the two central columns of the computation grid (Fig. 1). This method does not affect the Alternate Direction Implicit (ADI) solving of the temperature and motion equations. Indeed, in order to keep the tri-diagonal forms of the

Numerical model of mid-ocean ridges

P. Machetel and
C. J. Garrido

Title Page	
Abstract	Introduction
Conclusions	References
Tables	Figures
◀	▶
◀	▶
Back	Close
Full Screen / Esc	
Printer-friendly Version	
Interactive Discussion	



inversion matrix we split, as necessary, the horizontal (x direction) or vertical (y direction) segments into shorter ones surrounding the location where the internal condition is applied. Then both ends of the segments are used by the algorithm as internal or external boundary conditions. The amplitudes of stream-function jumps, located on the two central columns of the computation grid, from the Moho to the upper lens level, now simulate the discharges of sills and lenses defining the hypothesized melt intrusion pattern (Fig. 1). Free-slip boundary conditions ($\omega = 0$) have been applied to the vorticity equation.

It is also necessary to add bottom, lateral and internal conditions to solve the temperature equation. In order to avoid arbitrary hypotheses on the thermal structure of the underlying mantle, we consider that the oceanic crust is embedded in a half-space cooling lithosphere for which the ridge temperature has been set to the melt intrusion temperature $T_{\text{Ridge}} = 1280^\circ\text{C}$ (Eq. 8).

$$T(x, y) = T_{\text{Ridge}} \operatorname{erf} \left(\frac{z}{2} \sqrt{\frac{\rho C_p V_p}{k_m |x|}} \right). \quad (8)$$

The injection of the sheeted dykes layer at the ridge axis is simulated, at the roof of the upper lens, by a stream function jump, which amplitude is equal to the flux of the sheeted dyke layer through the left and right boundaries (Fig. 1). On the two central columns of the computation box, the stream function increases linearly from the roof of the upper lens to the surface. Then, for the horizontal rows corresponding to the sheeted dyke layer, starting from these two central points and going respectively to the right and left lateral boundary, the value of the stream-function is kept constant to ensure a horizontal velocity equal to the plate spreading. The thermal behavior of the sheeted dyke layer is simulated by an instantaneous freezing at the ridge axis. The zero value of the radial velocity inside of this layer ensures that the vertical heat transfer through the sheeted dyke layer is only conductive.

Numerical model of mid-ocean ridges

P. Machel et al.
C. J. Garrido

Title Page	
Abstract	Introduction
Conclusions	References
Tables	Figures
◀	▶
◀	▶
Back	Close
Full Screen / Esc	
Printer-friendly Version	
Interactive Discussion	



Second-order accuracy, ADI finite-difference schemes have been applied to solve the Laplace operators for stream-function, vorticity and temperature (e.g. Douglas and Rachford, 1956) with a 100×600 nodes grid corresponding to a 6×40 km oceanic crust areas. The computational process solves iteratively the vorticity, stream-function and temperature equations until the maximum relative evolution of the temperature between two time steps falls below 10^{-7} for each node of the computational grid.

3 Introducing the crust physical properties

We also need to describe the links between viscosity, thermal conductivity, hydrothermal cooling and the temperature, continuity and motion equations. In order to minimize the accuracy losses that may results from numerical differentiation, the local variations of the physical parameters have been written as hyperbolic, tangent-like Γ step functions (Eq. 9). Such functions, their derivatives and potencies are continuous and display accurate analytical expressions, evolving from 0 to 1. With this formalism, 88 % of the transition occurs over a 2δ range, centered on a threshold value, d_T . The quantity d may stand either for distances, temperatures or crystallization. Table 1 recalls the characteristic values used for the various physical parameter of this study. Most of them are still in the hart of scientific debates but, if we consider that the chosen values are representative of what could by the reality of oceanic crust properties, we do pretend that they are the most representative of the truth. However they allow illustrating the sensitivity of the numerical model to the assumptions and the uncertainties about the physical values and processes that affect the ocean ridge dynamics.

$$\Gamma(d) = \frac{1}{2} \left(1 + \tanh \left(\frac{d - d_T}{\delta} \right) \right). \quad (9)$$

Hence, in the following, we will consider that the melt fraction varies rapidly around a threshold temperature, $T_c = 1230^\circ\text{C}$, with a transition width $\delta T_c = 60^\circ\text{C}$ (Eq. (10) and Fig. 2 top). We chose to link the viscosity to crystallisation through Eq. (11) because

GMDD

6, 2429–2456, 2013

Numerical model of mid-ocean ridges

P. Machetel and
C. J. Garrido

Title Page

Abstract

Introduction

Conclusions

References

Tables

Figures

◀

▶

◀

▶

Back

Close

Full Screen / Esc

Printer-friendly Version

Interactive Discussion



Numerical model of mid-ocean ridges

P. Machel et al.
C. J. Garrido

Title Page

Abstract

Introduction

Conclusions

References

Tables

Figures

◀

▶

◀

▶

Back

Close

Full Screen / Esc

Printer-friendly Version

Interactive Discussion

several authors have emphasized such steepness for the viscosity variations with crystallization (e.g. Pinkerton and Stevenson, 1992; Marsh, 1996, 1998; Ishibashi and Sato, 2007). Such hypothesis could be easily modified in the numerical code where small changes in the description of physical dependencies of viscosity could be taken into account in a simple subroutine without changing the resolution scheme of the vorticity equation. In this work, we have assumed a viscosity ranging between a strong, cold phase for 0 % melt fraction ($\eta_s = 5 \times 10^{15}$ Pas) and a weak, hot phase for 100 % melt fraction ($\eta_w = 5 \times 10^{12}$ Pas or $\eta_w = 5 \times 10^{13}$ Pas). The two curves in the lower panel of Fig. 2 displays the resulting viscosity-temperature relationship according to the contrast of viscosity assumed between the strong and weak phases. Two viscosity contrasts, 5×10^{12} versus 5×10^{15} and 5×10^{13} versus 5×10^{15} (Pas) have been studied but, in the following, we will not show the results obtained for the temperature fields and the stream-function with the first viscosity jump because they are close are impossible to distinguish by eyes on the figures.

$$\Gamma_{\text{Cryst}}(x, y) = \frac{1}{2} \left(1 + \tanh \left(\frac{T(x, y) - T_{\text{Cryst}}}{\delta T_{\text{Cryst}}} \right) \right), \quad (10)$$

$$\eta(x, y) = \eta_w \Gamma_{\text{Cryst}}(x, y) + \eta_s (1 - \Gamma_{\text{Cryst}}(x, y))^3. \quad (11)$$

Hyperbolic, tangent-like Γ step functions have also been used to simulate hydrothermal cooling by linking the enhancement of thermal conductivity to depth and temperature. First we consider, through Eq. (12), that k decreases with depth from a high value, k_H near the surface, to a low value k_L at the Moho (numerical values are given in Table 1). Then we also assume, through Eq. (13), that conductivity depends on a cracking temperature T_{crack} , for which low (700 °C) and high (1000 °C) values have been tested. The resulting thermal conductivity that is used by the numerical model solving the

temperature equation is obtained through Eq. (14), combining Eqs. 12 and 13.

$$k_{\text{Depth}}(y) = k_L + (k_H - k_L) \frac{y}{H}, \quad (12)$$

$$\Gamma_{\text{Crack}}(x, y) = \frac{1}{2} \left(1 + \tanh \left(\frac{T(x, y) - T_{\text{Crack}}}{\delta T_{\text{Crack}}} \right) \right), \quad (13)$$

$$k(x, y) = k_L \Gamma_{\text{Crack}}(x, y) + k_{\text{Depth}}(1 - \Gamma_{\text{Crack}}(x, y)). \quad (14)$$

The dashed and solid lines of Fig. 2 (middle panel) displays the variation of thermal conductivity obtained at the surface level ($y = H$) according to the values assumed for the cracking temperature. The two series of cases corresponding to both cracking temperature assumptions will be shown in the following.

4 Effects of the accretion on the thermal and dynamic states of the ridge

In this work, three series of cases have been computed in order to illustrate the potential effects of the melt intrusion geometry. The first is a gabbro glacier structure (called G in the following); the second is a mixed structure with two lenses below the sheeted dyke and above the Moho (so-called M); and the third (so-called S) is a sheeted sill structure with superimposed sills delivering melt at the ridge axis. Our G consists of a melt intrusion through a shallow lens located just below the sheeted dyke (4.5 km above the MTZ). The M structure assumes two shallow and deep lenses respectively located just below the sheeted dyke and a few hundreds of meter above the MTZ (0.3 km and 4.5 km above the MTZ). Finally, the melt delivered for the S structure comes through nine sills, evenly stacked at the ridge axis, every 0.45 km, above the MTZ. Figure 3 displays the temperature patterns (color palette) and the stream functions isocontours (black lines) obtained for the low cracking temperature ($T_{\text{crack}} = 700^\circ\text{C}$) and with G, M and S melt intrusion hypotheses respectively in the top, middle and bottom panels. At a first glance, the stream-functions near the ridge reveal the different trajectories resulting from the accretion scenarios. As expected, the G structure (Fig. 3, top) induces

Numerical model of mid-ocean ridges

P. Machel et al.
C. J. Garrido

Title Page

Abstract

Introduction

Conclusions

References

Tables

Figures

⏪

⏩

◀

▶

Back

Close

Full Screen / Esc

Printer-friendly Version

Interactive Discussion



predominantly descending gabbro motion near the ridge axis. For the M structure, the melt is partly descending from the upper lens and partly rising from the MTZ lens (Fig. 3, middle) while, for the S structure the numerous superimposed intrusive sills induce nearly horizontal motion near the ridge axis (Fig. 3, bottom). The dynamics of the flow near the ridge are susceptible to modify the near ridge temperature field through the advection terms of the energy equation and the temperature dependence of viscosity in the vorticity equation. As a matter of fact, the transitions from G, M to S structures correspond to small effects that are difficult to interpret on the isotherms near the ridge axis (Fig. 3). Far from the ridge, the influence of the melt intrusion patterns on the temperature and motion damp rapidly to converge toward conductive temperature profiles and laminar flows.

A second series of cases has been calculated with a higher cracking temperature (1000 °C) for gabbros in order to try to illustrate the impact of the depth of hydrothermal cooling penetration in the crust. With a higher cracking temperature, the efficiency of hydrothermal cooling reaches a deeper layer and results in temperature colder by a few °C than in the previous cases (Fig. 4). However, the thermal effect remains small for the cases presented here. From a dynamic point of view, the results, displayed on Fig. 4 remain strongly dependent on the G, M or S structure hypotheses and similar to the ones previously obtained with a lower cracking temperature: the near-ridge gabbro motion is predominantly descending for the G structure (Fig. 4, top); is partly descending and partly rising for the M structure (Fig. 4, middle); and nearly horizontal for the S structure (Fig. 4, bottom). We also retrieved the same slight widening trends near the ridge.

5 Thermal history and cooling of the lower crust

The algorithm calculates the thermal histories of cooling gabbro in the lower crust by computing tracer (time-temperature) trajectories at the end of each run thanks to the steady states reached for velocities and temperature. The temperature versus time

range at $T_O = 1275^\circ\text{C}$ and to close it at the lowest temperature of melt solidus $T_C = 1125^\circ\text{C}$ (Table 1). For SCR, the opening temperature as been set to $T_O = 1050^\circ\text{C}$ and the closure temperature to $T_C = 850^\circ\text{C}$. According to the main locations of the 1275–1125 and 1050–850 $^\circ\text{C}$ isotherms in Figs. 3 and 4, ICR will be more sensitive to the thermal structure near the ridge axis while the SCR will mainly record the thermal structure a few kilometers off-axis.

Petrologists have studied the variations of cooling rates with depth in the plutonic crust of the Oman ophiolite and active mid-ocean ridges. Absolute quantitative cooling rates of the plutonic crust have been determined by thermochronology (John et al., 2004) and geospeedometry (Coogan et al., 2002, 2007; VanTongeren et al., 2008). Studies of the Crystal Size Distribution (CSD) of plagioclase in crustal gabbro have provided relative proxies for the variation of cooling rates with depth (Garrido et al., 2001). However, each of these cooling rates obtained from petrographic and/or mineral compositional data are characteristic of a opening-closure temperature range intrinsic to the methodology used. Hense CSD of plagioclase in plutonic rocks (Marsh, 1988, 1998) records the cooling dynamic of crystallization and hence are comparable to IRC. Conversely, cooling rates based on the subsolidus exchange of Ca between olivine and clinopyroxene (Coogan et al., 2002, 2005) mostly record cooling rate in a colder temperature interval, over which exchange diffusion is effective, providing hence SCR.

The left panel of Fig. 6 presents the ICR profiles obtained for the three series of cases while the right panel gives the result for the SCR profiles. Red, green and blue curves correspond respectively to the G, M and S ridge structure hypotheses. The results obtained with viscosity contrasts of two orders of magnitude and cracking temperatures $T_{\text{crac}} = 1000^\circ\text{C}$ have been drawn using heavy lines; the viscosity contrast of three orders of magnitude with cross symbols; and the viscosity contrast of two orders of magnitude but $T_{\text{crac}} = 700^\circ\text{C}$ with dashed lines. The comparisons of solid and cross shaped curves in Fig. 6 confirm that increases of two to three orders of magnitude for the viscosity contrasts have almost no effect on the cooling rates. In all the cases, the cross symbols superimpose almost perfectly with the corresponding heavy curves.

Numerical model of mid-ocean ridges

P. Machetel and
C. J. Garrido

[Title Page](#)[Abstract](#)[Introduction](#)[Conclusions](#)[References](#)[Tables](#)[Figures](#)[⏪](#)[⏩](#)[◀](#)[▶](#)[Back](#)[Close](#)[Full Screen / Esc](#)[Printer-friendly Version](#)[Interactive Discussion](#)

Numerical model of mid-ocean ridges

P. Machetel and
C. J. Garrido

Title Page

Abstract

Introduction

Conclusions

References

Tables

Figures

⏪

⏩

◀

▶

Back

Close

Full Screen / Esc

Printer-friendly Version

Interactive Discussion



Secondly, the comparisons of solid line curves with dashed lines provide visualizations of the effects of the cracking temperature level. In the previous section, comparing Figs. 3 to 4, we emphasized that the final effects of the cracking temperature on the global thermal patterns of solutions were small. Nevertheless, the slight trajectories and temperature distortions due to these changes modify the cooling rates of Fig. 6. The slightly colder environments, induced by the enhancement of the deep, near ridge cooling with the high cracking temperature contexts expose the gabbro to lower temperatures and therefore to higher rates of cooling. However, these effects remain weak and the slopes of the cooling rates curves with depth remain almost unchanged.

The effects of cracking temperature levels are similar but even less pronounced on the SCR profiles (Fig. 6, right panel). In these cases, the lower values of the opening-closure temperature range move the sampling of the lower crust toward areas close to conductive temperature and laminar motions. As a result, the differences in the cooling rates are reduced and the curves gather.

As a consequence, the effects of the G, M and S intrusion hypotheses on the cooling rate appear more clearly on the ICR (Fig. 6, left). The profiles are monotonic for the G structures (red curves), display bi-modal shapes with marked minimum values at the levels where the flows from the upper and lower lenses merge for the M structure and present saw tooth-like shapes for the S structures where the sills merge. The same analysis is difficult to apply to SCR profiles (Fig. 6, right) for which the shift of the sampled areas far from the ridge and the lower value of the closure temperature prevent from calculating the cooling rates in the lower part of the lower crust. It seems that the ability of SCR to differentiate the various accretion scenarios is reduced while ICR record the near ridge situation.

6 Summary and discussion

The new version of our thermo-mechanical model may be useful to explore the effects of deep, near off-axis hydrothermal cooling, variable melt supply geometry and

viscosity contrast on the thermal and dynamic patterns of flow near fast spreading mid ocean ridges. The series of cases presented in this paper simulate G, M or S ridge structures, with various viscosity contrasts and, through the effects of a cracking temperature, various depths of hydrothermal cooling. The similarity of thermal structures obtained for the G, M and S hypotheses, indicates they may be difficult to use them directly to discriminate between different crustal accretion scenarios. Indeed, all the cases investigated in this paper are finally consistent with geophysical data at EPR as reported by Dunn et al. (2000) and Singh et al. (2006): a 8–12 km wide magma chamber ($T < 1150^{\circ}\text{C}$) presenting steep isotherms near the ridge axis.

However, the combination of the near-ridge flow patterns with temperature may induce significant discrepancies in the cooling histories of gabbro and the ICR cooling rates calculated from the model seem able to discriminate among the different scenarios for the ridge accretion. It seems that it is no more the case with the SCR for which the lower opening-closure temperature range shifts the sampling of thermal pattern far from the ridge axis where laminar motions and conductive temperature become prominent. These simple behavior differences between ICR and SCR indicate that the assumption they could be similar in the same plutonic crust may be biased (Coogan et al., 2002, 2007; VanTongeren et al., 2008). We also would like emphasized that monotonic depth variations of the cooling rates are not necessarily symptomatic of conductive cooling and G ridge structure as proposed by Coogan et al. (2002) since it seems to be also the case for the S melt intrusion geometry. However, the significant variability observed among the petrological results for SCR results; and the significant differences that can be observed with the ICR profiles show the difficulty of drawing conclusions about the mechanism of accretion on this basis.

Garrido et al. (2001) measured CSD from plagioclase in the Khafifah section of the Wadi Tayin massif and found evidence of a transition from conduction dominated cooling in the lower gabbros (below 1500 m bove Moho) to hydrothermally dominated cooling in the upper gabbros (above 2500 m). They concluded theirs data were consistent with the S model of accretion. However, theirs cooling profiles did not show the same

GMDD

6, 2429–2456, 2013

Numerical model of mid-ocean ridges

P. Machellet and
C. J. Garrido

Title Page

Abstract

Introduction

Conclusions

References

Tables

Figures



Back

Close

Full Screen / Esc

Printer-friendly Version

Interactive Discussion



kind of evolution with depth than the present numerical study. They were displaying upper crust value 1.5 to 2 times faster than lower crust values. To the light of the present numerical results, this could be compatible with the three accretion structure hypotheses.

5 Coogan et al. (2002), using the Ca diffusion in olivine from Wadi Abyad massif crustal section reported that cooling rates decrease rapidly with depth by several orders of magnitude between the top and bottom of the lower crust. They also mention that the cooling depth profile matches that of conductive models. These authors concluded in favor of a crystallisation occurring inside of the magmatic chamber and hence a G ridge structure. Van Tongeren et al. (2008) extended the work of Coogan et al. (2002) in the Wadi Tayin massif of the Oman ophiolite. The two studies differ both in amplitudes and shapes of cooling rates profiles (see the comparison in Fig. 7 of VanTongeren et al. (2008) and Fig. 3 of MacLennan et al., 2005). Van tongeren et al. (2008) argued that these differences reflect distinct thermal histories due to differences in crustal thickness and/or the geodynamic setting. However, the Wadi Abyad cooling rates recalculated by VanTongeren et al. (2008) using Coogan's data (Coogan et al., 2002) remain several orders of magnitude faster than the ones calculated by the former. Such differences between the results of Van Tongeren (2008) and those of Cogan et al. (2002) suggest, as recalled by Coogan et al. (2002) and Mac Lennan et al. (2005), that large uncertainties in petrological SCR may probably come from a deficit of constraints on the values of diffusion parameters. The SCR computed with our model in the lower crust for the G, M and S structures fall within the broad range of the petrological cooling rates of Coogan et al. (2002). They also display slopes agreeing, at least for the lower crust, with those computed by Van Tongeren et al. (2008) and Cherkaoui et al. (2003) results.

25 In spite and because of these uncertainties, our results suggest that numerical modeling of ICR and SCR may provide essential tools to discriminate between different crustal accretion scenarios of fast spreading mid-ocean ridges.

GMDD

6, 2429–2456, 2013

Numerical model of mid-ocean ridges

P. Machetel and
C. J. Garrido

Title Page

Abstract

Introduction

Conclusions

References

Tables

Figures

⏪

⏩

◀

▶

Back

Close

Full Screen / Esc

Printer-friendly Version

Interactive Discussion



Supplementary material related to this article is available online at:
[http://www.geosci-model-dev-discuss.net/6/2429/2013/
gmdd-6-2429-2013-supplement.zip](http://www.geosci-model-dev-discuss.net/6/2429/2013/gmdd-6-2429-2013-supplement.zip).

Acknowledgements. We thank Jill VanTongeren for kindly sharing data on cooling rates from the Oman ophiolite. Lawrence Coogan, John McLennan and Tim Henstock whose comments that have greatly contribute to improve the manuscript and the numerical model.



The publication of this article is financed by CNRS-INSU.

References

- Bédard, J. H. and Hebert, R.: The lower crust of the Bay of Islands ophiolite, Canada Petrology, mineralogy, and the importance of syntexis in magmatic differentiation in ophiolites and at ocean ridges, *J. Geophys. Res.-Sol. Ea.*, 101, 25105–25124, 1996.
- Bosch, D., Jamais, M., Boudier, F., Nicolas, A., Dautria, J. M., Agrinier, P.: Deep and high-temperature hydrothermal circulation in the Oman ophiolite – petrological and isotopic evidence, *J. Petrol.*, 45, 1181–1208, 2004.
- Boudier, F. and Nicolas, A.: Nature of the Moho transition zone in the Oman Ophiolite, *J. Petrol.*, 36, 777–796, 1995.
- Boudier, F., Nicolas, A., and Ildefonse, B.: Magma chambers in the Oman ophiolite: fed from the top and the bottom, *Earth Planet. Sci. Lett.*, 144, 239–250, 1996.
- Boudier, F., Godard, M., and Armbruster, C.: Significance of noritic gabbros in the gabbro section of the Oman ophiolite, *Mar. Geophys. Res.*, 21, 307–326, 2000.
- Chen, Y. J.: Thermal effects of gabbro accretion from a deeper second melt lens at the fast spreading East Pacific Rise, *J. Geophys. Res.-Sol. Ea.*, 106, 8581–8588, 2001.

Numerical model of mid-ocean ridges

P. Machetel and
C. J. Garrido

Title Page

Abstract

Introduction

Conclusions

References

Tables

Figures



Back

Close

Full Screen / Esc

Printer-friendly Version

Interactive Discussion



Numerical model of mid-ocean ridges

P. Machel and
C. J. Garrido

Title Page

Abstract

Introduction

Conclusions

References

Tables

Figures

◀

▶

◀

▶

Back

Close

Full Screen / Esc

Printer-friendly Version

Interactive Discussion



- Chenevez, J., Machel, P., and Nicolas, A.: Numerical models of magma chambers in the Oman ophiolite, *J. Geophys. Res.-Sol. Ea.*, 103, 15443–15455, 1998.
- Cherkaoui, A. S. M., Wilcock, W. S. D., Dunn, A. R., and Toomey, D. R.: A numerical models of hydrothermal cooling and crustal accretion at a fast spreading mid-ocean ridge, *Geochem. Geophys. Geosys.*, 4, 8616, doi:10.1029/2001GC000215, 2003.
- Coogan, L. A., Jenkin, G. R. T., and Wilson, R. N.: Constraining the cooling rate of the lower oceanic crust: a new approach applied to the Oman ophiolite, *Earth Planet. Sci. Lett.*, 199, 127–146, 2002.
- Coogan, L. A., Hain, A., Stahl, S., and Chakraborty, S.: Experimental determination of the diffusion coefficient for calcium in olivine between 900 degrees C and 1500 degrees C, *Geochim. Cosmochim. Ac.*, 69, 3683–3694, 2005.
- Coogan, L. A., Howard, K. A., Gillis, K. M., Bickle, M. J., Chapman, H., Boyce, A. J., Jenkin, G. R. T., and Wilson, R. N.: Chemical and thermal constraints on focused fluid flow in the lower oceanic crust, *Am. J. Sci.*, 306, 389–427, doi:10.2475/06.2006.01, 2006.
- Coogan, L. A., Jenkin, G. R. T., and Wilson, R. N.: Contrasting cooling rates in the lower oceanic crust at fast- and slow-spreading ridges revealed by geospeedometry, *J. Petrol.*, 48, 2211–2231, 2007.
- Crawford, W. C. and Webb, S. C.: Variations in the distribution of magma in the lower crust and at the Moho beneath the East Pacific Rise at 9 degrees–10 degrees N, *Earth Planet. Sci. Lett.*, 203, 117–130, 2002.
- DeMartin, B., Hirth, G., and Evans, B.: Experimental constraints on thermal cracking of peridotite at oceanic spreading centers, *Mid-Ocean Ridges : Hydrothermal Interactions between the lithosphere and Oceans*, *Geophys. Monogr. Ser.* 148, 167–186, 2004.
- Douglas, J. and Rachford, H. H.: On the numerical solution of heat conduction problems in two and three space variables, *Trans. Am. Math. Soc.*, 82, 966–968, 1956.
- Dunn, R. A., Toomey, D. R., and Solomon, S. C.: Three-dimensional seismic structure and physical properties of the crust and shallow mantle beneath the East Pacific Rise at 9° 30' N, *J. Geophys. Res.-Sol. Ea.*, 105, 23537–23555, 2000.
- Garrido, C. J., Kelemen, P. B., and Hirth, G.: Variation of cooling rate with depth in lower crust formed at an oceanic spreading ridge: Plagioclase crystal size distributions in gabbros from the Oman ophiolite, *Geochem. Geophys. Geosys.*, 2, 1041, doi:10.1029/2000GC000136, 2001.

Numerical model of mid-ocean ridges

P. Machetel and
C. J. Garrido

Title Page

Abstract

Introduction

Conclusions

References

Tables

Figures

◀

▶

◀

▶

Back

Close

Full Screen / Esc

Printer-friendly Version

Interactive Discussion

- Marsh, B. D.: Crystal size distribution (CSD) in rocks and the kinetics and dynamics of crystallization – I. Theory, *Contrib. Mineral. Petrol.*, 99, 277–291, 1988.
- Marsh, B. D.: Solidification fronts and magmatic evolution, *Mineralog. Mag.*, 60, 5–40, 1996.
- Marsh, B. D.: On the interpretation of crystal size distributions in magmatic systems, *J. Petrol.*, 39: 553–599, 1998.
- 5 Nedimovic, M. R., Carbotte, S. M., Harding, A. J., Detrick, R. S., Canales, P., Diebold, J. B., Kent, G. M., Tischer, M., and Babcock, J. M.: Frozen magma lenses below the oceanic crust, *Nature*, 436, 1149–1152, 2005.
- Nicolas, A., Boudier, F., and Ceuleneer, G.: Mantle flow patterns and magma chambers at ocean ridges – evidence from the Oman ophiolite, *Mar. Geophys. Res.*, 9, 293–310, 1988.
- 10 Nicolas, A., Freydier, C., Godard, M., and Boudier, F.: Magma chambers at oceanic ridges: how large?, *Geology*, 21, 53–5, 1993.
- Phipps Morgan, J. and Chen, Y. J.: The genesis of oceanic-crust, magma injection, hydrothermal circulation, and crustal flow, *J. Geophys. Res.-Sol. Ea.*, 98, 6283–6297, 1993.
- 15 Pinkerton, H. and Stevenson, R. J.: Methods of determining the rheological properties of magmas at sub-liquidus temperatures, *J. Volc. Geoth. Res.*, 53, 47–66, 1992.
- Quick, J. E. and Denlinger, R. P.: Ductile deformation and the origin of layered gabbro in ophiolites, *J. Geophys. Res.*, 98, 14015–14027, 1993.
- Schouten, H. and Denham, C.: Virtual ocean crust, *Trans AGU EOS*, 76, p. S48, 1995.
- 20 Singh, S. C., Harding, A. J., Kent, G. M., Sinha, M. C., Combier, V., Tong, C. H., Pye, J. W., Barton, P. J., Hobbs, R. W., White, R. S., and Orcutt, J. A.: Seismic reflection images of the Moho underlying melt sills at the East Pacific Rise, *Nature*, 442, 287–290, 2006.
- Sinton, J. M. and Detrick, R. S.: Mid-ocean ridge magma chambers, *J. Geophys. Res.*, 97, 197–216, 1992.
- 25 Sleep, N. H.: Formation of oceanic crust: some thermal constraints, *J. Geophys. Res.*, 80, 4037–4042, 1975.
- Theissen-Krah, S., Lyer, K., Rüpke, L. H., and Phipps Morgan, J.: Coupled mechanical and hydrothermal modeling of crustal accretion at intermediate to fast spreading ridges, *Earth Planet. Sci. Lett.*, 311, 275–286, 2011.
- 30 VanTongeren, J. A., Kelemen, P. B., and Hanghoj, K.: Cooling rates in the lower crust of the Oman ophiolite: Ca in olivine, revisited, *Earth Planet. Sci. Lett.*, 267, 69–82, 2008.

Table 1. Notations and values used in this paper.

Notations	Name (Units)	Values
Fluid velocity	v (m s^{-1})	
Horizontal coordinate (offset from ridge)	x (m)	$-L$ to L
Vertical coordinate (height above Moho)	y (m)	0 to H
Vertical coordinate (depth below seafloor)	z (m)	0 to H
Temperature	T ($^{\circ}\text{C}$)	
Pressure	ρ (N m^{-2})	
Strain	τ (N m^{-2})	
Stream function	ψ ($\text{m}^2 \text{s}^{-1}$)	
Vorticity	ω (s^{-1})	
Time	t (s)	
Density	ρ (kg m^3)	
Latent heat of crystallization	Q_L (J kg^{-1})	500×10^3
Heat capacity by unit of mass	C_p ($\text{J kg}^{-1} \text{K}^{-1}$)	10^3
Gravity acceleration	g ($\text{m}^2 \text{s}^{-1}$)	
Crystallization function	Γ_{Cryst} (-)	0 to 1
Thermal conductivity	k (J (m s K)^{-1})	
High thermal conductivity	k_{h} (J (m s K)^{-1})	20.0
Low thermal conductivity	k_{l} (J (m s K)^{-1})	2.5
Low Cracking temperature	$T_{\text{Crac}}(\text{K}; ^{\circ}\text{C})$	973; 700
High Cracking temperature	$T_{\text{Crac}}(\text{K}; ^{\circ}\text{C})$	1273; 1000
Cracking temperature interval	$T_{\text{Crac}}(\text{K}; ^{\circ}\text{C})$	60; 60
Dynamic viscosity	η (Pa s)	
Weak viscosity (weak phase)	η_w (Pa s)	5×10^{12} or 5×10^{13}
Strong viscosity (strong phase)	η_s (Pa s)	5×10^{15}
Mid crystallization temperature	$T_{\text{Cryst}}(\text{K}; ^{\circ}\text{C})$	1503; 1230
Crystallization temperature interval	$\delta T_{\text{Cryst}}(\text{K}; ^{\circ}\text{C})$	60; 60
Crust thickness from Moho to sea floor	H (m)	6000
Distance from ridge to lateral box boundary	L (m)	20000
Right and left symmetric spreading plate velocity	V_p (m s^{-1} ; m yr^{-1})	1.5844×10^{-9} ; 5×10^{-2}
Ridge temperature for lithospheric cooling	$T_{\text{Ridge}}(\text{K}; ^{\circ}\text{C})$	1553; 1280
Lens height above Moho	Y_l (m)	4500
Total lineic ridge discharge	$\psi_{\text{e}}(\text{m}^2 \text{s}^{-1})$	1.9013×10^{-5}
Stream function left bottom boundary	$\psi_{\text{lb}}(\text{m}^2 \text{s}^{-1})$	0.9506×10^{-5}
Stream function lateral left boundary	$\psi_{\text{l}}(\text{m}^2 \text{s}^{-1})$	
Stream function top boundary	$\psi_{\text{t}}(\text{m}^2 \text{s}^{-1})$	0
Stream function lateral right boundary	$\psi_{\text{r}}(\text{m}^2 \text{s}^{-1})$	
Stream function right bottom boundary	$\psi_{\text{rb}}(\text{m}^2 \text{s}^{-1})$	-0.9506×10^{-5}
Seafloor temperature	$T_{\text{sea}}(\text{K}; ^{\circ}\text{C})$	273; 0
Melt intrusion temperature	$T_{\text{Melt}}(\text{K}; ^{\circ}\text{C})$	1553; 1280
Opening temperature for ICR (liquidus)	$T_{\text{O}}(\text{K}; ^{\circ}\text{C})$	1548; 1275
Closure temperature for ICR (solidus)	$T_{\text{C}}(\text{K}; ^{\circ}\text{C})$	1398; 1125
Opening temperature for SCR	$T_{\text{O}}(\text{K}; ^{\circ}\text{C})$	1323; 1050
Closure temperature for SCR	$T_{\text{C}}(\text{K}; ^{\circ}\text{C})$	1123; 850
Number of horizontal grid points	N_x (grille1; grille 2)	600; 1798
Number of vertical grid points	N_y (grille1; grille 2)	100; 298

Numerical model of mid-ocean ridges

P. Machetel and
C. J. Garrido

Title Page

Abstract

Introduction

Conclusions

References

Tables

Figures

◀

▶

◀

▶

Back

Close

Full Screen / Esc

Printer-friendly Version

Interactive Discussion



Numerical model of mid-ocean ridges

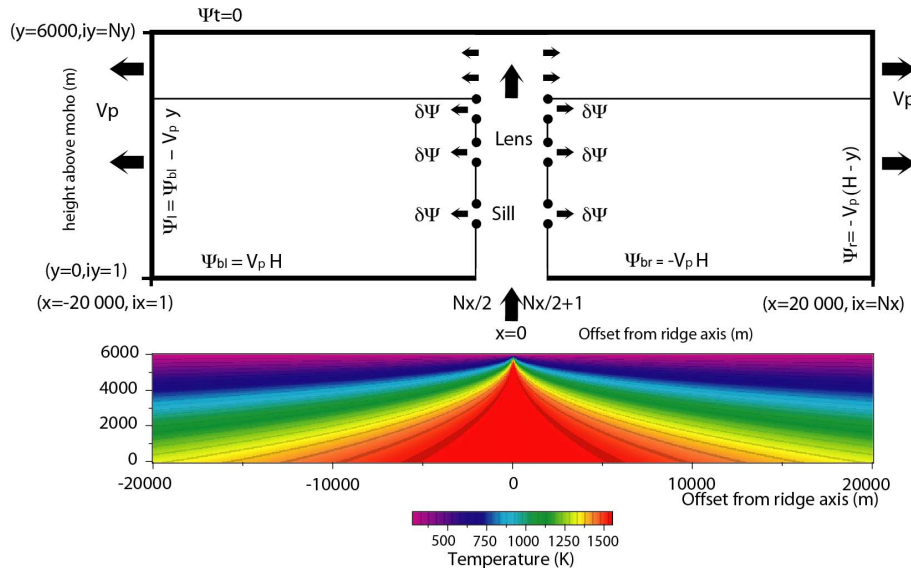
P. Machetel and
C. J. Garrido

Fig. 1. Sketch of the stream-function (top) and temperature (bottom) internal and boundary conditions. The computation grid is composed of N_x vertical columns (from 1 to N_x , $x = -L$ to $x = L$) and N_y rows (from 1 to N_y , $y = 0$ to $y = H$). The ridge axis is located between the points $N_x/2$ and $(N_x/2) + 1$ where the amplitude of the stream-function jump is equal to $\Psi_c = 2V_p H$, the total flux of crust that leaves the computation box through the left and right lateral boundaries. At the top of the crust and at the Moho level, Ψ is constant (impervious boundary), except at the ridge axis. Its bottom left value has been set to $\Psi_{bl} = V_p H$. Internal stream function jumps, $\delta\Psi$, on the two central columns, drive the melt intrusion through sills and/or lenses. Initial and internal boundary conditions are also applied to the temperature field according to a half-space lithospheric cooling law (Eq. 14).

Title Page

Abstract

Introduction

Conclusions

References

Tables

Figures

◀

▶

◀

▶

Back

Close

Full Screen / Esc

Printer-friendly Version

Interactive Discussion



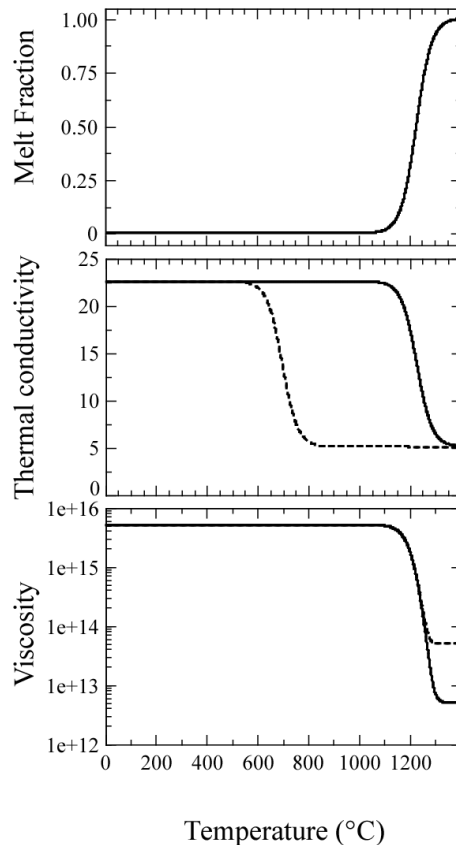


Fig. 2. top: Amplitude of the melt fraction Γ_{Cryst} versus temperature; middle: thermal conductivity k at the surface of the model (dashed curve: $T_{\text{Crac}} = 700^\circ\text{C}$; solid curve: $T_{\text{Crac}} = 1000^\circ\text{C}$); bottom: dynamic viscosity η versus temperature (dashed curve: $\eta_w = 5 \times 10^{13}$ Pas, solid curve: $\eta_w = 5 \times 10^{12}$ Pas).

Numerical model of mid-ocean ridges

P. Machetel and
C. J. Garrido

Title Page

Abstract

Introduction

Conclusions

References

Tables

Figures

◀

▶

◀

▶

Back

Close

Full Screen / Esc

Printer-friendly Version

Interactive Discussion



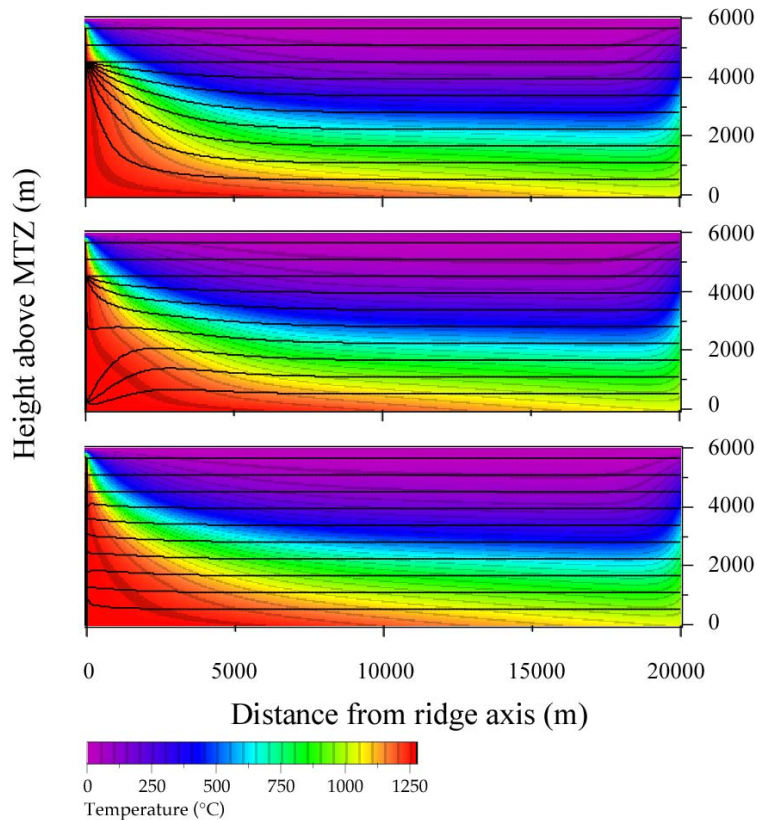


Fig. 3. Temperature fields and stream function isocontours obtained for the G (top), M (middle) and S (bottom) ridge structures. The direction of velocity is directly given by the stream-function. The results have been obtained with a hydrothermal cracking temperature $T_{\text{crac}} = 700\text{ }^{\circ}\text{C}$ and a viscosity contrast of two orders of magnitudes.

Numerical model of mid-ocean ridges

P. Machetel and
C. J. Garrido

Title Page

Abstract

Introduction

Conclusions

References

Tables

Figures

◀

▶

◀

▶

Back

Close

Full Screen / Esc

Printer-friendly Version

Interactive Discussion



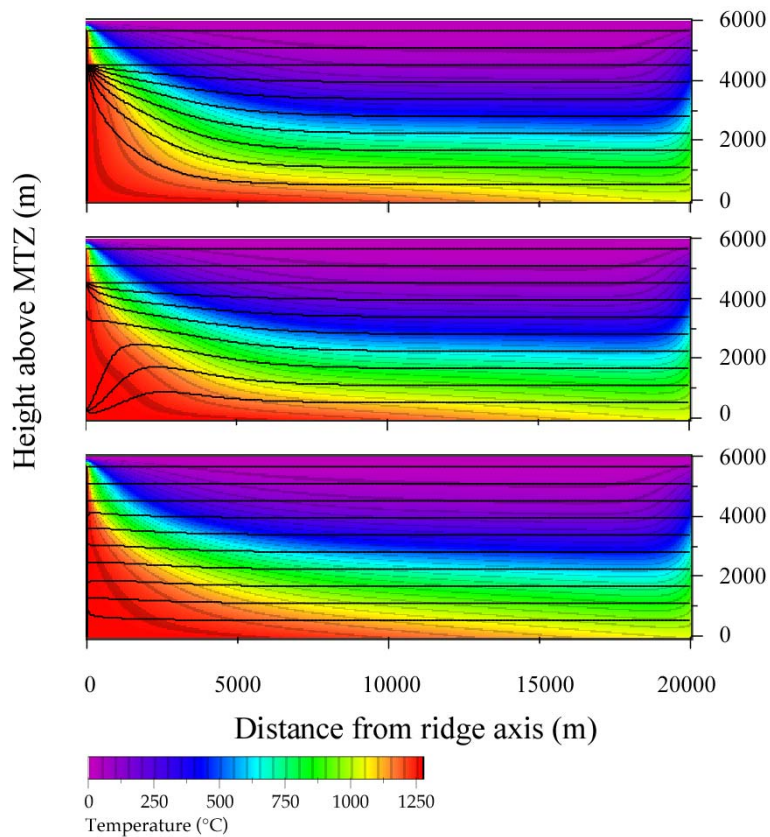


Fig. 4. Same as Fig. 3 for a hydrothermal cracking temperature $T_{crac} = 1000^\circ\text{C}$.

Numerical model of mid-ocean ridges

P. Machetel and
C. J. Garrido

Title Page

Abstract

Introduction

Conclusions

References

Tables

Figures

◀

▶

◀

▶

Back

Close

Full Screen / Esc

Printer-friendly Version

Interactive Discussion



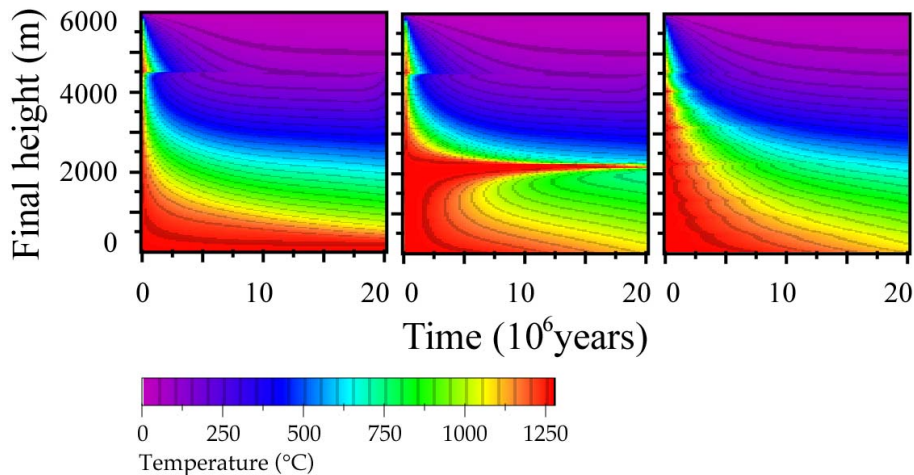


Fig. 5. Thermal history of the gabbro versus their final height above MTZ in the lower crust for the G (left), M (middle) and S (right) ridge accretion hypothesis. The results have been obtained with $T_{\text{crac}} = 700^\circ\text{C}$.

Numerical model of mid-ocean ridges

P. Machetel and
C. J. Garrido

Title Page

Abstract

Introduction

Conclusions

References

Tables

Figures

◀

▶

◀

▶

Back

Close

Full Screen / Esc

Printer-friendly Version

Interactive Discussion



Numerical model of mid-ocean ridges

P. Machetel and
C. J. Garrido

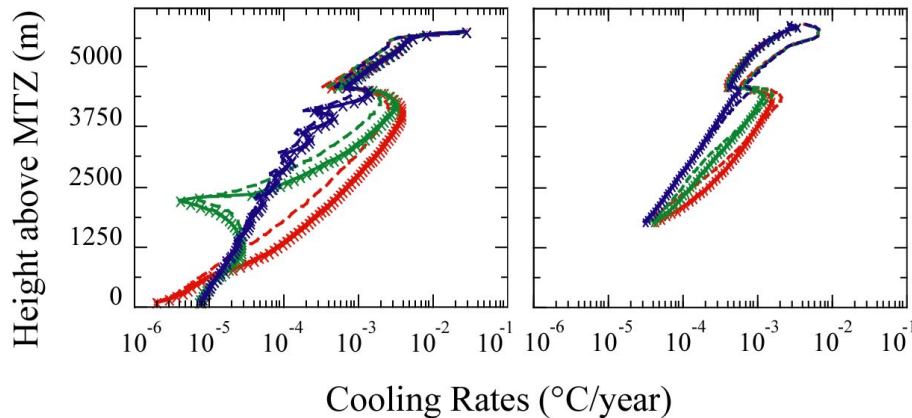


Fig. 6. Igneous cooling rates ICR (left panel) and Subsolidus cooling rates SCR (right panel) versus final crustal depths for the G (red curves), M (green curves) and S (blue curves) ridge accretion hypotheses. In each panel, heavy solid lines correspond to cases with two orders of magnitude viscosity contrasts and high cracking temperature (1000 °C). The cases obtained by changing the viscosity contrasts superimpose perfectly (X symbols). Finally, the results obtained with a lower hydrothermal cracking temperature of 700 °C are displayed with dashed line.

[Title Page](#)
[Abstract](#)
[Introduction](#)
[Conclusions](#)
[References](#)
[Tables](#)
[Figures](#)
[⏪](#)
[⏩](#)
[◀](#)
[▶](#)
[Back](#)
[Close](#)
[Full Screen / Esc](#)
[Printer-friendly Version](#)
[Interactive Discussion](#)
